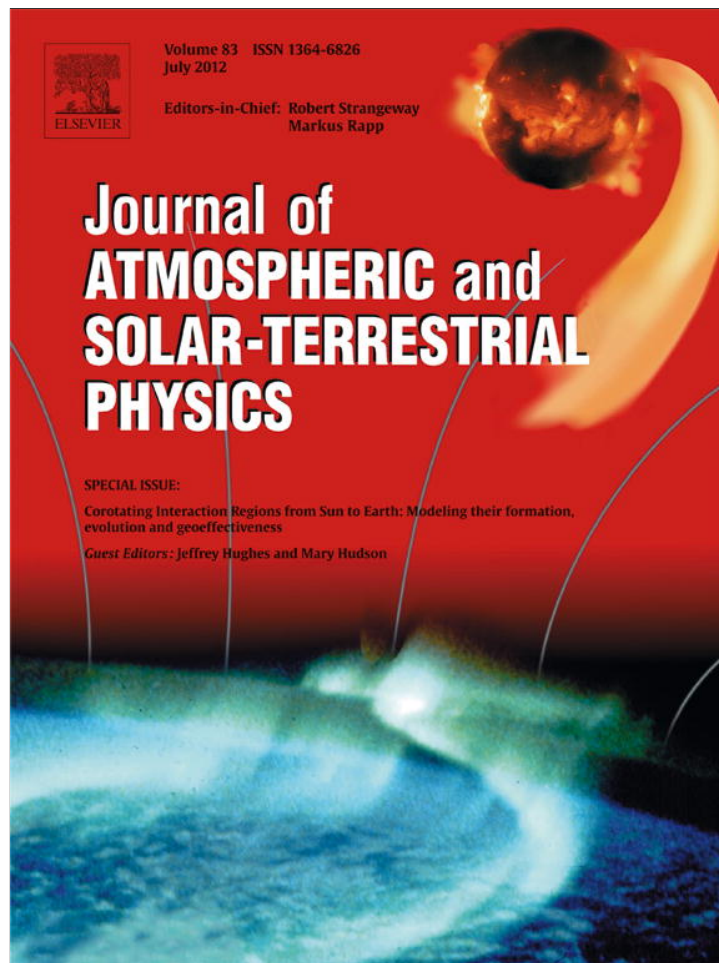


Provided for non-commercial research and education use.
Not for reproduction, distribution or commercial use.



This article appeared in a journal published by Elsevier. The attached copy is furnished to the author for internal non-commercial research and education use, including for instruction at the authors institution and sharing with colleagues.

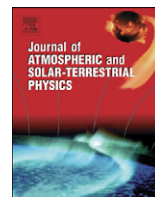
Other uses, including reproduction and distribution, or selling or licensing copies, or posting to personal, institutional or third party websites are prohibited.

In most cases authors are permitted to post their version of the article (e.g. in Word or Tex form) to their personal website or institutional repository. Authors requiring further information regarding Elsevier's archiving and manuscript policies are encouraged to visit:

<http://www.elsevier.com/copyright>

Contents lists available at [SciVerse ScienceDirect](http://www.sciencedirect.com)

Journal of Atmospheric and Solar-Terrestrial Physics

journal homepage: www.elsevier.com/locate/jastp

Interpreting some properties of CIRs and their associated shocks during the last two solar minima using global MHD simulations

Pete Riley ^{a,*}, Jon A. Linker ^a, J. Americo Gonzalez Esparza ^b, L.K. Jian ^c, C.T. Russell ^c, J.G. Luhmann ^d

^a Predictive Science, Inc., 9990 Mesa Rim Road, San Diego, California, United States

^b Unidad Michoacán, Instituto de Geofísica Universidad Nacional Autónoma de México, México

^c UCLA, Los Angeles, California, United States

^d UCB, Berkeley, California, United States

ARTICLE INFO

Article history:

Received 1 September 2011

Received in revised form

28 January 2012

Accepted 31 January 2012

Available online 9 February 2012

Keywords:

Corona

Solar wind

Corotating interaction regions

Magnetohydrodynamics

Space weather

ABSTRACT

In this study, we investigate some properties of corotating interaction regions (CIRs) during the recent solar minimum (December 2008), and compare them to CIRs observed during the previous minimum (September 1996). In particular, we focus on the orientation of stream interfaces (SIs), which separate wind that was originally slow and dense from wind that was originally fast and tenuous. We find that while the east–west flow deflections imply a systematic tilt of CIRs such that they are aligned with the nominal Parker spiral direction, the north–south flow deflections are much more irregular and show no discernible patterns. Comparison with global MHD model results suggest that this is a consequence of the spacecraft intercepting the equatorward flanks of the CIRs. We also study the solar-cycle variations of CIR-associated shocks over the last cycle, finding that forward (F) shocks tended to occur approximately three times more frequently than reverse (R) shocks, and, moreover, during the recent minimum, there were approximately 3–4 times more R shocks than during the previous minimum. We show that this too is likely due to the orientation of CIRs and Earth's limited vantage point in the ecliptic plane.

© 2012 Elsevier Ltd. All rights reserved.

1. Introduction

Corotating interaction regions (CIRs) are large-scale structures in the solar wind produced primarily by the rotation of the Sun. Interaction regions, in general, occur where parcels of plasma traveling radially out from the Sun at different speeds interact (Sarabhai, 1963). Where slower wind is caught by faster wind, a compression region forms, bound by forward (F) and reverse (R) waves. Conversely, where faster wind outruns slower wind, a rarefaction or expansion wave forms. Usually, the term “interaction region” refers to the compression region, although strictly speaking, rarefaction regions are also sites of interaction. The boundary that separates what was originally slow and dense wind from what was originally fast and tenuous within a compression region is referred to as the stream interface (SI) (Burlaga, 1974). SIs also occur within rarefactions/expansion waves, but typically can only be discerned through composition signatures (Wimmer-Schweingruber et al., 1997).

The properties of CIRs have been investigated for more than 45 years, since the bimodal speed structure of the solar wind was

first reported (Neugebauer and Snyder, 1966; Belcher and Davis, 1971). In a landmark paper, Gosling et al. (1978) comprehensively described the plasma properties of abrupt SIs using a superposed epoch analysis. Amongst their results, they found: (1) SIs separate wind that was originally dense and slow from wind that was originally fast and tenuous; (2) the SI is a location of shear flow; (3) SI speeds tend to be $< 450 \text{ km s}^{-1}$; and (4) a discontinuous rise in the α abundance ratio occurs at the interface, suggesting distinct origins for the flows on either side of the SI. Later, Gosling (1995) and Riley et al. (1996) studied the tilts of CIRs at mid heliographic latitudes, during the declining phase of solar cycle 22 using measurements from the Ulysses mission. Riley et al. (1996), in particular, studied the properties of the F and R shocks bounding the CIRs, finding that shock strength appeared to be modulated by the tilt of the solar dipole, peaking at latitudes roughly equivalent to the maximum extent of the heliospheric current sheet (HCS). Additionally, they found that F shocks were oriented such that they propagated equatorward and westward, while R shocks propagated poleward and eastward, suggesting that the CIRs were systematically tilted in the heliosphere. These results were confirmed by looking at the global flow deflections through the CIR.

The F and R shocks associated with CIRs have also been studied for many decades both from analysis of *in situ* measurements

* Corresponding author. Tel.: +1 8582175868; fax: +1 8584501953.
E-mail address: pete@predsci.com (P. Riley).

(Sonett and Colburn, 1965) and inferences from 1-D (Hundhausen, 1973), 2-D (Pizzo, 1981), and 3-D (Pizzo, 1982) numerical models. Early 1-D simulations suggested that F and R shocks formed at approximately the same time, thus implying that, since the F shock was farther away from the Sun than the R shock, that R shocks would be preferentially observed at a given distance from the Sun, at least until a few AU, by which time both would presumably have fully developed.

In this study, we focus on two specific properties of CIRs and their associated shocks. In a previous investigation, Jian et al. (2011) presented a comprehensive analysis of both CIR and CME structures observed at 1 AU in the ecliptic plane over the last solar cycle. In particular, they produced a comprehensive list of SIs and CIR-associated structures, including F and R shocks, which act as the starting point for the present analysis. First, we investigate the flow deflections occurring at SIs both during the recent minimum and the previous one. From these, we compute the orientation of the SIs. Second, we analyze the occurrence rate of both F and R CIR-associated shocks through solar cycle 23. To understand these results, we analyze global MHD solutions for the same time periods, focusing our discussion here on the recent minimum.

This recent solar minimum, “agreed by panel” to have occurred in December 2008 (NOAA/SWPC, 2011) but more generally considered to be defined by an interval rather than a point in time (Gibson et al., 2011), appears to have been unique in a number of ways, at least within the time span of a century (Phillips, 2009). In particular, there were marked differences in the structure of the solar wind during the minimum marking the end of solar cycle 22 (September 1996) and the most recent minimum, marking the end of solar cycle 23 (December 2008) (Emery et al., 2009; Riley et al., 2010, 2011; Gibson et al., 2011). At least in part, these differences were likely driven by a reduced polar photospheric flux, which was lower by $\approx 40\%$ (Svalgaard and Cliver, 2007), producing polar coronal holes that were noticeably smaller (Kirk et al., 2009), and more equatorial coronal holes (Riley et al., 2011). Also related to the unique distribution of magnetic flux in the photosphere was the ubiquitous presence of unipolar (pseudo-) streamer structure during much of the recent minimum interval (Riley and Luhmann, 2011). In previous studies, we investigated the large-scale structure of the inner heliosphere using global MHD models at these two minima (e.g., Riley et al., 2001, 2010), comparing them with *in situ* measurements from ACE and Ulysses.

2. Techniques for estimating the orientation of CIRs/SIs

A number of techniques have been developed for inferring the orientation of SIs, CIRs, and the shocks associated with them. Siscoe (1972) applied a variance analysis to the velocity vectors across five stream interfaces, associating the direction of minimum variance with the normal to the SI. González-Esparza and Smith (1997) extended this technique to account for the fact that while the direction of maximum variance can be unambiguously identified with the plane of the SI, there is ambiguity about the orientations of the intermediate and minimum variance directions, and that the minimum variance direction does not necessarily lie parallel to the SI normal.

Here, we introduce perhaps the simplest method for inferring the orientations of SIs. It has the limitation that meaningful results can only be derived for cases with clear signatures present. More complicated techniques, such as that described by González-Esparza and Smith (1997) can be used to confirm these basic results. However, and as noted by González-Esparza and Smith (1997), while employing the more sophisticated techniques will always yield a result, one must still visually inspect the

measurements and compare them with the output from the technique to show that they are robust.

Fig. 1 illustrates how flow is deflected at a SI where fast solar wind is catching up to slower wind ahead. It is important to note that these flows are in the frame of the SI that is moving radially out with the solar wind. In this case, the orientation of the interface is such that fast wind is deflected northward and eastward as it approaches the SI while slower wind flowing back into the SI is deflected westward and southward. The lower panels of Fig. 1 recast these flow deflections in terms of what a spacecraft would measure as the structure passed over it. In this case, the spacecraft is not measuring the lagrangian flow (that is, following a parcel of plasma), but rather the Eulerian flow (at a fixed point). Thus, the instrument first measures essentially radial slow flow ahead of the SI. As the SI approaches, the flow is seen to deflect southward and westward. The spacecraft then intercepts the SI, which it sees as a discontinuous change in flow direction, and becomes immersed in the deflected fast wind, which flows northward and eastward. Far enough from the SI, the flow returns to the radial direction.

In Fig. 2 we have simplified the geometry at the stream interface showing slices in the equatorial and meridional planes. Assuming that the flow into the SI is initially radial, we can use the following relations to compute the azimuthal and meridional tilts of the SI:

$$\tan(\Phi) = \frac{v_t}{v_r} \quad (1)$$

$$\tan(\Theta) = \frac{v_r}{v_n} \quad (2)$$

where (v_r, v_t, v_n) are the velocity components in the RTN coordinate system. In this coordinate system, \mathbf{e}_r points radially away from the Sun, \mathbf{e}_t points in the direction of planetary motion and lies in the equatorial plane, and \mathbf{e}_n completes the system.

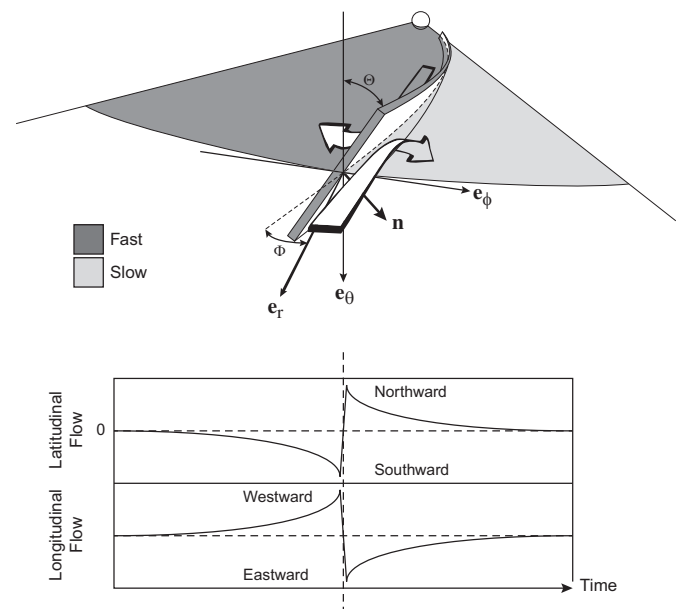


Fig. 1. (Top) An illustration of the flow patterns into and away from a stream interface, in a frame moving with the interface (Adapted from Pizzo, 1991). Fast flow to the east overtakes slower flow to the west and is deflected northward and eastward. Slow wind flows toward the Sun radially and is deflected southward and westward. (Bottom) Schematic flow deflections that would be measured by a spacecraft as the stream interfaced passed over it. Initially slow, radial wind is sampled, which acquires a progressively larger southward and westward component. The spacecraft then passes over the SI (dashed vertical line) and samples the faster wind, which initially contains a large northward and eastward component and progressively diminishes farther away from the interface.

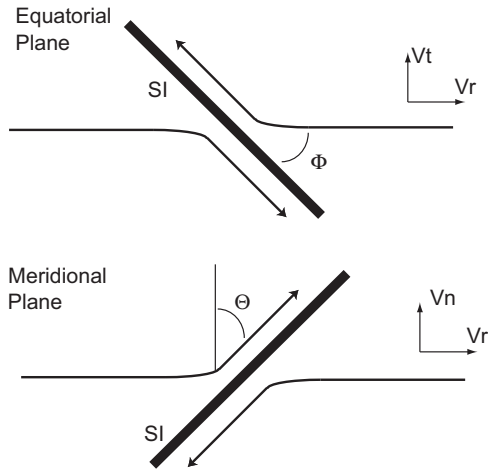


Fig. 2. (Top) A schematic illustrating the flow patterns in the (top) equatorial plane and (bottom) meridional plane. The deflections, θ and ϕ , are also shown, together with the relevant RTN velocity components.

(In effect, \mathbf{e}_n points in the direction of \mathbf{e}_θ and \mathbf{e}_t points in the direction of \mathbf{e}_ϕ , where θ and ϕ are the standard angles in the spherical coordinate system.) Using a solar rotation period of $\tau_{rot} = 25.38$ days, we would predict that an interface traveling at 429 km s^{-1} would be tilted in azimuth by 45° . Similarly, speeds of 350 km s^{-1} and 600 km s^{-1} would produce tilts of 55° and 35° , respectively. This makes sense intuitively, since as the speed of the solar wind increases, the Parker spiral angle it makes with the radial should decrease. We also note that from Eq. (2) that, in the limit that $v_n \rightarrow 0$ on both sides of the SI, $\theta \rightarrow 90^\circ$, and the SI lies perpendicular to the radial direction, in the meridional plane. To reiterate, the main assumptions of this technique are that: (1) Far from the SI, the flow is radial; and (2) the flow deflections are symmetric in amplitude about the SI.

3. Analysis of the stream interfaces

In a previous study, Jian et al. (2011) identified and catalogued the basic properties of CIRs during solar cycle 23, that is, from 1995 through 2009, which itself was an extension of CIR survey covering 1995–2004 (Jian et al., 2006). They found the CIRs were more prevalent during the recent minimum (occurring at the end of solar cycle 23, December 2008) than during the previous one (September 1996). They also noted the presence of more CIR-associated shocks, which they attributed to different ambient properties of the solar wind during the recent minimum, leading to a lower fast magnetosonic wave speed of the solar wind. Our analysis here builds on these results by investigating the orientation of the SIs observed during solar cycle 23 as well as the occurrence rate of CIR-associated shocks during this same period.

Between 1995 and 2009, Jian et al. (2011) identified 577 CIRs. Since some of them did not recur from one rotation to the next, they were collectively named stream interaction regions, or SIRs, rather than CIRs; however, for simplicity, we will retain the latter term. Jian et al. (2011) used the following criteria to identify CIRs: an overall speed increase; peaks in total pressure (Russell et al., 2005) and proton number density; an increase in temperature; a change in entropy; flow deflections; and field enhancement. The SI itself was chosen to be the point where the total pressure peaked. From the full list, they further identified 36 CIRs with sharp stream boundaries.

In this study, we focus primarily on the orientation of the SIs embedded within these 36 CIRs. We describe two events in detail (one from 1995 (event ‘A’) and one from 2009 (event ‘B’)), which

capture the general features of most of the SIs studied, and summarize the properties of the remaining ones. In Fig. 3, we show bulk solar wind speed (v), latitudinal and longitudinal flow angles, plasma density (N), and magnetic field strength (B) for the event A. The flow deflections are in the same coordinate system as in Figs. 1 and 2, such that a positive (negative) latitudinal flow is northward (southward) and a positive (negative) longitudinal flow is westward (eastward). The magnetic field strength has been color-coded according to the polarity of the interplanetary magnetic field (IMF). The central dashed line marks the location of the SI as determined by Jian et al. (2011), and the two bounding lines show the intervals used to assess the orientation of the SI. These intervals were chosen subjectively such that they captured the large-scale flow patterns associated with the SI, and in particular, any local maxima, but not so broad that they were contaminated by other dynamical processes. We note several points. First, the SI separates what was originally slow-flowing wind from what was initially fast-flowing wind (Gosling et al., 1978). Before it, slow wind has been accelerated and after it, fast wind has been decelerated. Second, asymmetric peaks in N and B occur at the SI: the bulk of the density enhancement occurring prior to the SI, and the bulk of the field strength enhancement occurring after it. The region of accelerated or decelerated flow stretches from the region of density enhancement before the SI to the region of field strength enhancement after it. Third, the longitudinal (or azimuthal) flow deflections about the SI are consistent with those in Fig. 1: the initially radial flow (0°) is first deflected to the west (positive) then abruptly to the east (negative) as the SI is crossed before returning to radial. Fourth, the latitudinal (meridional) flow deflections are very small and show little change, in particular organized by the SI crossing. Moreover, there is no obvious change at the SI. Fifth, the polarity of the IMF changes 3.75 days before the SI is crossed, marking the traversal of the HCS.

Our second example comes some 14 years later. In Fig. 4 we show the same parameters as in Fig. 3 for an SI observed on day 284, 2009 (event ‘B’). With a few differences, the profiles for this event are very similar to event A. The bulk flow profile, longitudinal flow deflections and asymmetric density and field strengths are all remarkably similar. The trailing portion of the field strength enhancement is longer and the latitudinal flow deflection, while also irregular, is suggestive of a small shift from negative (southward) to positive (northward) values across the SI.

Focusing on the longitudinal flow deflections for both events, we can use Eq. (2) to infer the orientation of the SI in the ecliptic plane. Although we could, in principle, pair values equidistant from the SI and compute and ensemble average, a simpler and arguably more robust approach is to estimate the largest flow deflection on either side and use the mean value of this pair to infer the azimuthal orientation of the SI, since our simple cartoon assumes that the deflections are symmetric with respect to the SI. Doing this for event A yielded $\phi = 29^\circ$ and $\theta = 9^\circ$. However, given the assumption of symmetric deflections of the opposite sense, we cannot rely on the determination for the orientation in θ . We also computed the variance matrix eigenvalues and eigenvectors for the interval surrounding the SI, finding that the minimum, intermediate, and maximum eigenvalues were 161, 364, and 17,849. Thus, as reported by González-Esparza and Smith (1997), while the maximum value is well determined, there is degeneracy in the minimum and intermediate values, suggesting the normal to the SI can be only localized to a plane, and not a direction.

Repeating this analysis for event B, we found minimum, intermediate, and maximum eigenvalues of 174, 272, and 1989, again underlining the degeneracy of the minimum and intermediate directions. Using Eqs. (1) and (2), we found $\phi = 41^\circ$ and $\theta = 10^\circ$.

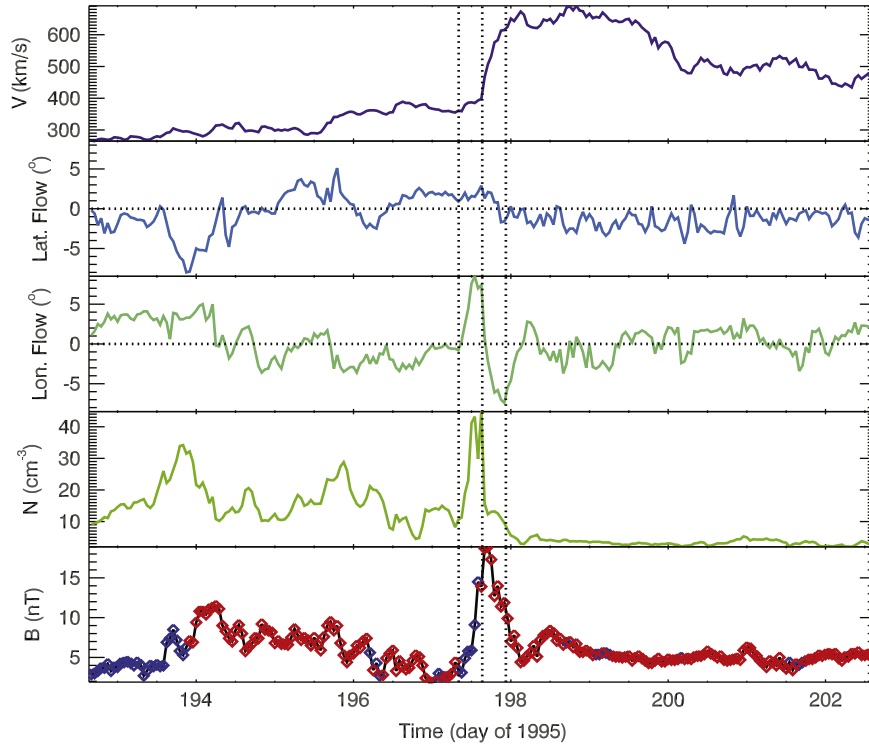


Fig. 3. Time series of bulk solar wind speed (v), latitudinal and longitudinal flow angles, solar wind density (N), and magnetic field strength (B) for an event on day 197 of 1995 (event 'A'). The field strength has been color-coded with the polarity of the interplanetary magnetic field, red indicating outward fields and blue indicating inward fields. The central vertical dashed line marks the location of the SI while the two adjacent vertical dashed indicate the upstream (left) and downstream (right) regions over which the analysis was performed.

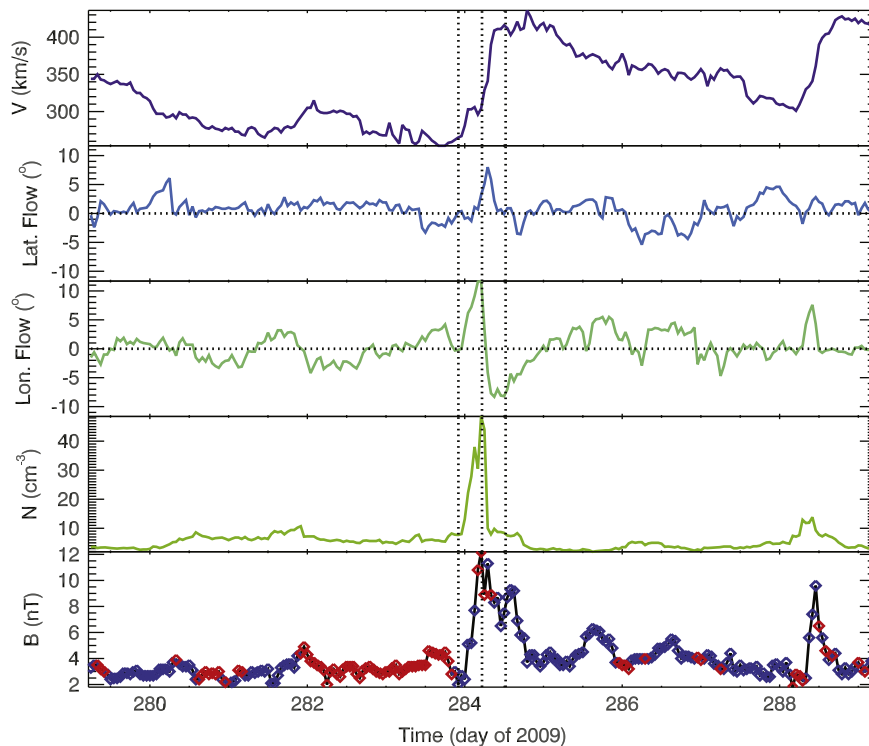


Fig. 4. As Fig. 3 for an SI on day 284 in 2009.

Again, we can only rely on the value determined for Φ , for which the time series meets the basic assumptions of the technique.

It is worth noting that we might anticipate that the azimuthal orientation of the SI would be intermediate between the Parker

spiral angles computed for the slow wind ahead of the SI and the fast wind behind it. For event A, for which the speeds of the slow and fast wind ahead of or behind the SI were $\sim 350 \text{ km s}^{-1}$ and $\sim 700 \text{ km s}^{-1}$, the nominal Parker spiral angles are 51° and 32° ,

respectively. Thus, our computed azimuthal orientation of 29° lies at the fast-speed end. For event B, for which the slow and fast wind were $\sim 200 \text{ km s}^{-1}$ and $\sim 450 \text{ km s}^{-1}$, the Parker spiral angles are 65° and 43° , respectively. Again, our computed angle of 41° lies very near the fast-speed orientation. We are cautious in interpreting these results, however: The orientations determined by Eq. (2) are sensitive to the window chosen. While there are well-determined maxima in the azimuthal flow deflections, and hence azimuthal speeds, the same is not true for the radial speeds, which continue to increase as the window boundaries are moved progressively further from the SI and beyond the peak amplitudes in the azimuthal flow.

Between 1995 and 2009, Jian et al. (2011) identified 36 SIs (or $\approx 20\%$ of the total number) with sharp boundaries where the proton number density and temperature changed rapidly. We analyzed each of these events individually as described above, removing a further six events that did not meet our criterion of sufficiently sharp gradient in speed with either a well-defined density or magnetic field enhancement. Of the remaining 30 events, 27 (90%) showed azimuthal deflections suggesting a shear flow, and discontinuity, in the same sense as in Fig. 1. Only four events (13%) showed a meridional profile as in Fig. 1; two in one sense, a positive deflection followed by a negative deflection, and two in the other sense. However, even for these events, the deflections were not as unambiguous as those for the azimuthal deflections shown in Figs. 3 and 4. In general, the meridional (latitudinal) deflections could be catalogued in the following way: Nine events (30%) displayed flows that drifted continuously through the SI; 10 events (33%) rose to a maximum deflection at the SI (either positive or negative) before returning to near zero; seven events (23%) remained approximately zero throughout the interval surrounding the SI; and three events (10%) were approximately constant, but offset from zero. The fact that the sum of these cases exceeds 30 indicates that there was ambiguity in the classification, and several of the events could be interpreted as being consistent with more than one category, depending on how wide one chose the window for analysis. Finally, no systematic differences were found between the SI properties during the two minima.

4. Analysis of the forward and reverse shocks

We now turn our attention to some properties of the F and R shocks bounding the CIRs observed during solar cycle 23. We note that there is not a one-to-one correspondence between these shocks and the SIs analyzed in the previous section: Some CIRs contain sharp SIs but do not drive shocks, while others drive shocks but do not contain sharp SIs. Again, we start from the study by Jian et al. (2011), who compiled a list of events from Wind and ACE measurements and summarized some of their properties. In particular, they found that, using the total pressure across the shock as a proxy for shock strength, the strength of CIR-associated shocks changed in phase with the solar cycle, being strongest at solar maximum, and weakest at solar minimum. They also concluded that there was no clear dependence on the occurrence rate of CIR-associated shocks with solar cycle, a result we will dispute. Finally, they found that, during the recent minimum, 39% of CIRs had shocks associated with them; more than double the rate for the previous minimum.

Here, we extend the analysis of Jian et al. (2011) to investigate the rate of occurrence of CIR-associated shocks, and the ratio of F to R shocks during the course of the solar cycle, the results of which are both interesting and, perhaps, unexpected. We then interpret the observations with the aid of numerical simulations.

In Fig. 5 we show the variability of F, R, and total CIR-associated shock rates (shocks/year) as a function of year for solar cycle 23. The monthly sunspot number is also shown to give a solar cycle context to the shock variations. Typically, there were ~ 8 – 17 shocks each year around solar minimum, and there was a tendency for the total shock rate to be smaller between 2000 and 2004 than at other times. Perhaps more remarkably, the shock rate was lowest in 2003–2004 during the early declining phase of solar cycle 23, a time typically associated with well-formed CIRs (Riley et al., 2001, 2002, 2003b). Considering the F and R shocks individually, while there was no obvious trend with respect to the F shocks, there was a tendency for more R shocks to be present around the recent minimum (December 2008) than the previous minimum (September 1996).

In Fig. 6, we show the ratio of F to R shocks as a function of solar cycle. In general, from 1998 onward, the ratio of F to R

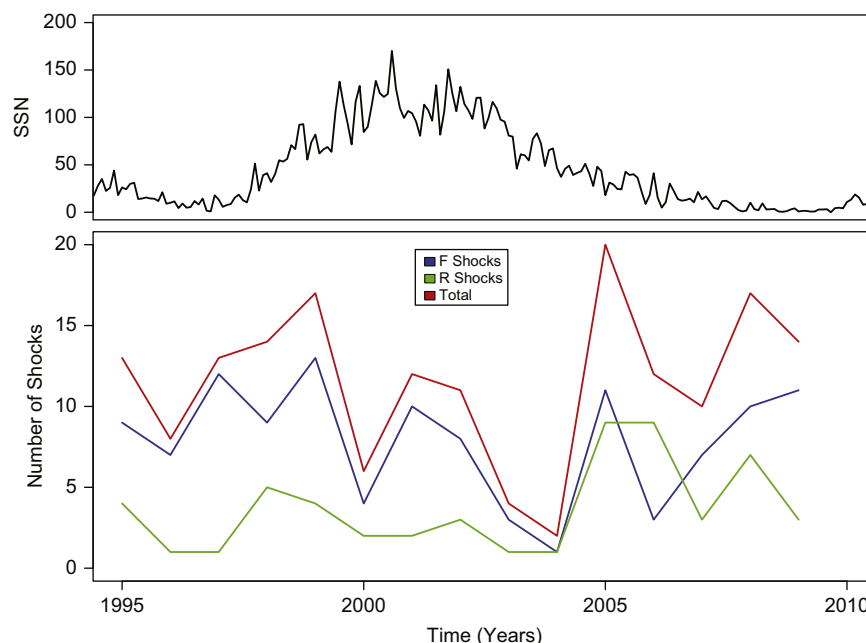


Fig. 5. (Top) The monthly averaged sunspot number as a function of time for the interval 1995–2009 (i.e., solar cycle 23). (Bottom) The annual number of all CIR-associated shocks (red), and forward (blue) and reverse (green) shocks separately. (For interpretation of the references to color in this figure legend, the reader is referred to the web version of this article.)

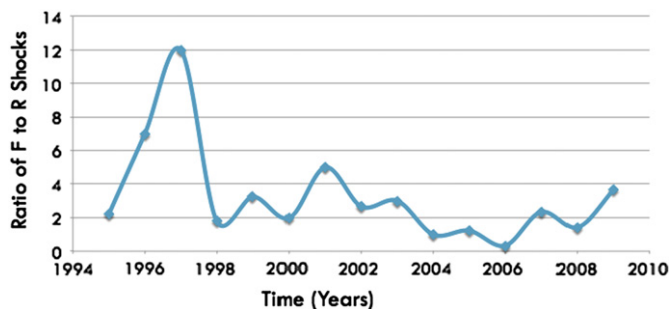


Fig. 6. The ratio of F to R shocks as a function of time for solar cycle 23.

shocks remained relatively stable at $\sim 2-3$, dipping below one only in 2006. However, in 1996 and 1997, the ratio was significantly higher. It is worth emphasizing, however, that in each of these years, only one R shock was observed; thus this peak should be viewed with caution.

5. Interpretation of CIR orientations and shock occurrence rates using global MHD models

Global magnetohydrodynamic (MHD) models of the solar corona and inner heliosphere can be a useful tool for interpreting the global structure associated with *in situ* measurements (e.g., Riley et al., 2001, 2003a). To provide genuine insight, however, the solutions must match the observations we are seeking to interpret. We have found that, in the absence of obvious transient activity, our ambient solar wind solutions do match observations reasonably well (Riley, 2010; Riley et al., 2011), although there remain a number of issues that must be resolved (Riley et al., *in press*). Here, we restrict our inferences from the model results to a statistical nature. In future studies, we plan to undertake a more detailed event by event comparison.

The modeling technique implemented here is described in more detail by Riley et al. (2001) and references therein. Here we make only a few brief comments. First, we use photospheric synoptic magnetograms to drive the model. This allows us to compute solutions for specific periods of interest, rather than generating idealized or generic solutions. Second, we employ an empirical coupling between the coronal and heliospheric models, which, while from a scientific perspective is not as desirable as a direct coupling, usually produces more accurate heliospheric solutions. Third, unlike other heliospheric models (e.g., Odstrcil et al., 2004) our code is more numerically tolerant approaching the solar poles, allowing us to compare model results directly with Ulysses high-latitude observations (Stevens et al., *submitted for publication*).

Although we solve the full set of resistive MHD equations, it is worth noting that, to a large extent, the properties of CIRs are controlled by the dynamic pressure of the solar wind. For example, assuming a plasma density of $n \sim 5 \text{ cm}^{-3}$, a bulk speed of $v \sim 500 \text{ km s}^{-1}$, a magnetic field strength of $B \sim 5 \text{ nT}$, and a proton temperature of $T \sim 10^4 \text{ K}$, we compute a dynamic pressure of $2 \times 10^{-9} \text{ Pa}$, a magnetic pressure of 10^{-11} Pa , and a thermal pressure of $3.5 \times 10^{-12} \text{ Pa}$. Thus, the dynamic pressure exceeds the magnetic pressure by a factor of 100 and exceeds the thermal pressure by a factor of 600. This is not to say that these contributions can always be ignored. We have considered the effects of neglecting the magnetic field and found that while the stream profiles are not significantly effected, there are notable differences in some cases (Riley et al., *in press*). The generic values we used to derive the pressures at 1 AU may also impact this conclusion. In the slow solar wind, the speed is smaller, and the

density and magnetic field strength are greater. However, even in such cases, the dynamic pressure continues to dominate. Finally, it is worth noting that since the dynamic pressure varies as $\sim nv^2$, and both density and speed typically vary by a factor of two between slow and fast wind, it is the velocity variations that have the primary effect in driving CIR structure.

In previous studies (Riley et al., 2010, 2011), we contrasted model solutions for Whole Sun Month (WSM) and Whole Heliosphere Interval (WHI), which occurred between August 8–September 4, 1996 and March 19–April 16, 2008, respectively, and thus illustrated the properties of the heliosphere near each of the last two minima (although the WHI interval might be better described as late-declining phase). We found that, in agreement with *in situ* measurements, the structure of the recent minimum was significantly more complex than during the WSM period, during which time CIRs were systematically tilted due to the simple tilted (or warped) velocity pattern back at the Sun. More recently, Riley et al. (*in press*) made detailed comparisons between MHD model results and *in situ* measurements for several intervals within the recent solar minimum, both to understand the structure of the large-scale structure of the inner heliosphere and assess the power and limitations of current modeling techniques.

In the present study, we consider the orientation of CIRs during the recent minimum in more detail. CR 2080, which occurred from February 10 through March 9, 2009, serves as a good illustration: It occurred within the broader time period identified as solar minimum (Gibson et al., 2011) and was devoid of any obvious transient activity, such as CMEs. In Fig. 7, we show the global meridional (latitudinal) and azimuthal (longitudinal) speeds, as well as thermal pressure at 1 AU. We note several points: (1) CIR structure is limited to latitudes of $\pm 40^\circ$; (2) two primary features are present – “streaks” that move from low latitudes toward the poles with increasing longitude, and “horseshoe” shaped structures centered about the heliographic equator; (3) azimuthal-speed “streaks” of opposite sign are paired up and located at the same latitudes; (4) similarly, meridional “streaks” are paired up too, however, in this case, the trailing (earlier longitude) lobe is displaced to higher latitudes.

In Fig. 8, we connect the locations of the CIRs with the flow deflections associated with them. The two panels again show meridional and azimuthal speed, however, with an iso-surface of pressure at some arbitrary level overlaid, identifying regions of compression. The locations of the CIRs obviously depends on which iso-surface is plotted. The value chosen here aimed to balance the identification of sufficient structure without complicating the display. From this we see that a spacecraft confined to within $\pm 7.25^\circ$ of the heliographic equator would likely observe systematic azimuthal deflections across a CIR (a spacecraft would appear to propagate from right to left in these plots, moving, at most a few degrees in latitude). On the other hand, while the spacecraft might measure deflections in latitude, these would be at best, of only one sign. Thus, in at least a statistical sense, we expect to see systematic azimuthal flow deflections indicating systematic tilts, but not in latitude. Moreover, it is possible to cut through CIR flanks and produce smooth variations in the latitudinal flow angle as well as asymmetric peaks (that is rising from zero to some maximum and then falling back to zero), or even some constant offset from zero, as observed in some events.

Finally, in Fig. 9, we show a complementary view of these structures in the meridional plane for four equally separated slices in longitude. Panels 1 and 3, in particular, illustrate the “streaks” of Figs. 7 and 8, which appear as compressions (bright regions) moving to higher latitudes with increasing distance from the Sun. At lower latitudes, the “horseshoe” structures appear as blobs in these displays. Based on these results, while we expect

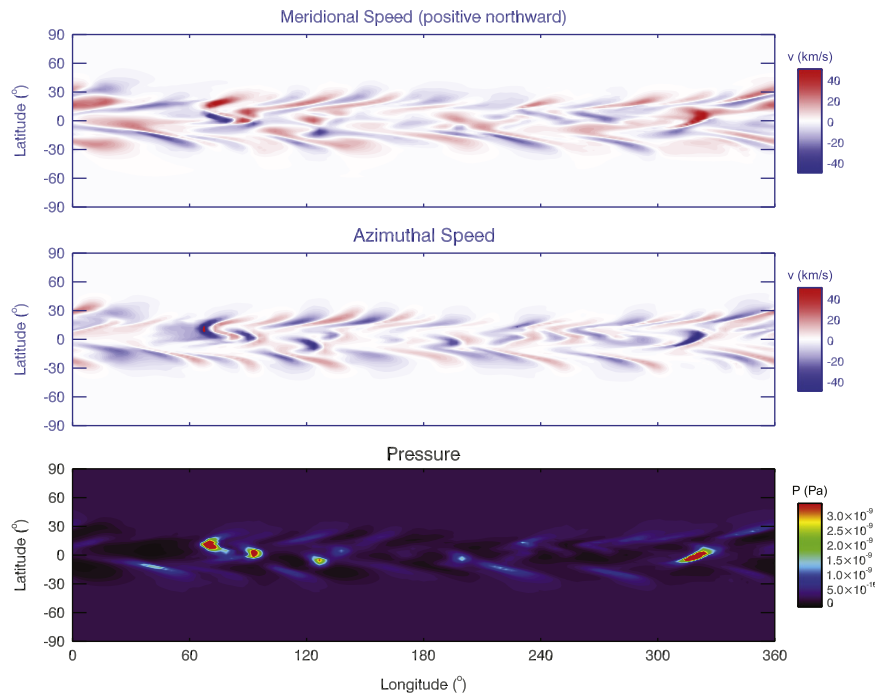


Fig. 7. (Top) Meridional speed, (middle) azimuthal speed, and (bottom) thermal pressure as a function of longitude and latitude at 1 AU for CR 2080.

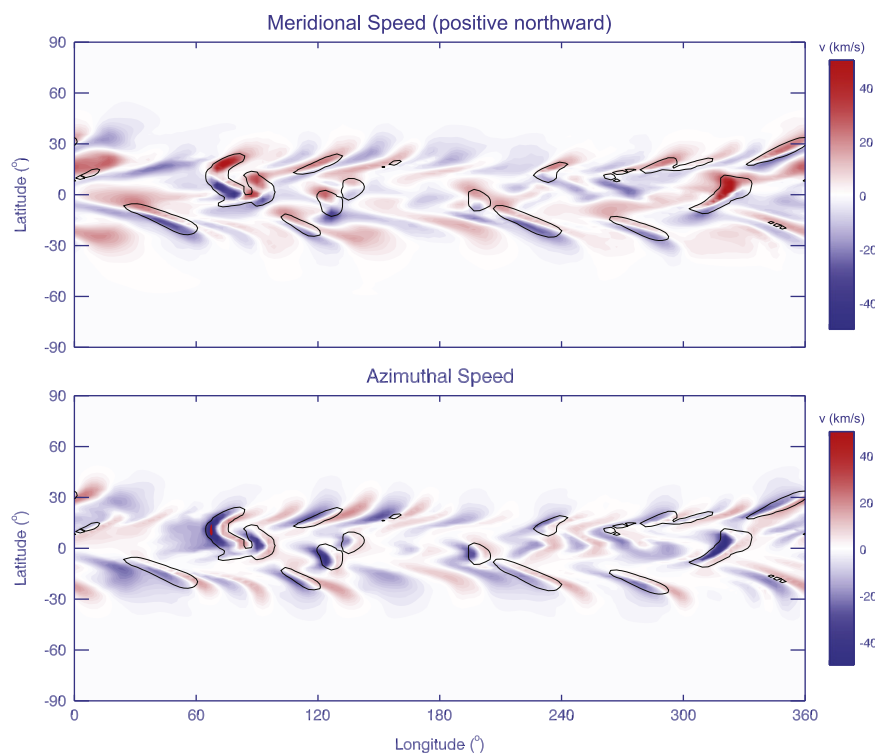


Fig. 8. (Top) Meridional speed (where positive is northward) and (bottom) azimuthal speed as a function of longitude and latitude at 1 AU for CR 2080. Overlaid are contours of thermal pressure at some arbitrary level marking the location of compression regions. These locations coincide with the high pressure regions in Fig. 7.

CIRs and SIs in particular, to be tilted at midlatitudes in the manner illustrated in Fig. 1, in the ecliptic plane, we would not expect to see any systematic tilts. Additionally, we would predict little to no deflections as the interface would lie roughly perpendicular to the radial direction in the meridional plane.

Based on these patterns, we can also suggest why more F than R shocks are observed in the ecliptic plane and why more R shocks were present during the recent minimum than the

previous one. In the left panel of Fig. 9, for example, F waves/shocks bound the two most prominent CIRs on the anti-sunward (or leading) side, while R waves/shocks bound the trailing side. As was shown by Gosling et al. (1995) in relation to Ulysses observations, this suggests F shocks are oriented with their outward normals pointing to the equator in both hemispheres, whereas the outward normals for the R shocks point toward the poles (and back to the Sun). The new aspect of this geometry for interpreting

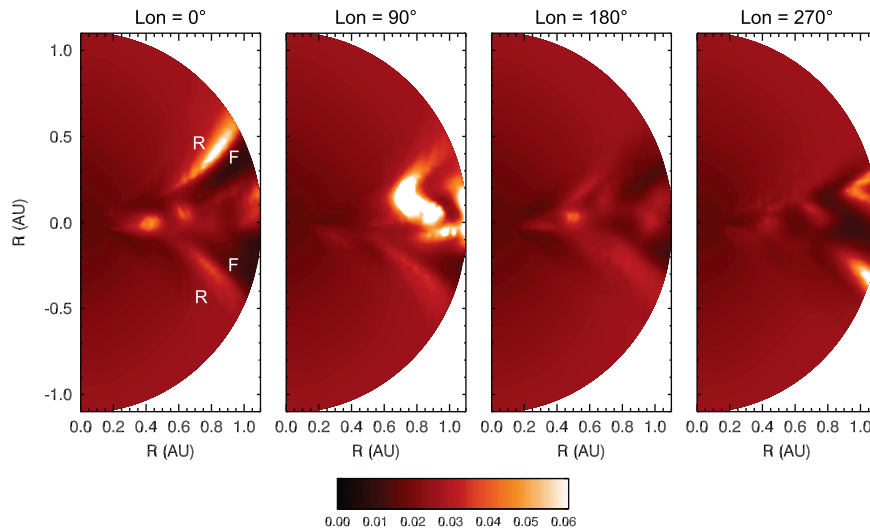


Fig. 9. Meridional cross-sections of scaled pressure at four longitudes for the same interval as Figs. 7 and 8. The pressure has been scaled with heliocentric distance by $r^{10/3}$. In the left-most panel two pairs of F/R waves/shocks have been labeled for illustration.

in-ecliptic measurements is that the flanks of the F shock stretch to lower latitudes than the R shock, because of the tilt of the CIRs. Thus, an in-ecliptic spacecraft sampling this structure (which, ignoring evolutionary effects could be approximated by a radial slice at constant latitude traveling back to the Sun) would be significantly more likely to intercept a F shock than a R shock. Moreover, the main difference between the structure in Figs. 7–9 and that present during the 1996 minimum (Riley et al., 2001) is the presence of the “horseshoe” shaped interaction regions produced by the equatorial coronal holes. These effectively increase the number of R shocks, relative to F shocks, during the recent minimum, and provide an explanation for the peak around 1997 in Fig. 6 (or from a different perspective, the lack of a bump during the most recent minimum).

6. Summary and discussion

In this study, we have analyzed the orientations of SIs during the most recent minimum (December 2008) as well as the previous one (1996), finding that, as previously reported, the east–west flow deflections show a systematic pattern that can be interpreted such that the interfaces are oriented along the nominal Parker spiral direction, with a pitch between that of the slow wind in front of it and the fast wind behind it (Gosling et al., 1978), although based on our analysis, more closely aligned with the fast wind. On the other hand, and as yet unreported, the north–south flow deflections revealed no obvious patterns. In fact, a significant fraction showed relatively little flow deflection near the SI, suggesting that they lay perpendicular to the radial direction in the meridional plane. Global numerical solutions, at least in a statistical sense, are consistent with these results. We suggest that while the Sun’s rotation drives the E–W orientations, the latitudinal distribution of solar wind velocity near the Sun drives the N–S orientations. We showed that during these intervals two primary types of interactions were being generated. First, the systematic tilts prevalent in the declining phase of solar cycle 22 (Riley et al., 1996) were occurring well beyond the vicinity of the equatorial (or ecliptic) plane and, thus, the interaction regions measured by Wind/ACE were from the flanks of structures that spanned tens of degrees in latitude. And second, equatorial coronal holes during the recent minimum produced interaction regions with little systematic tilt in the meridional plane, and also increased the relative proportion of R shocks during this time.

The differences observed in the rate of occurrence of R shocks between the recent and previous minima could be explained by the properties of the high-speed streams, which, during the recent minimum were found to be stronger, of longer duration, and more recurrent, at least through the late declining phase (Gibson et al., 2011). On the other hand, as Jian et al. (2011) pointed out, the shock rate could have been modulated by the ambient wind conditions. In particular, the ease at which a shock can form is related to the local magnetosonic speed. Lower this and a pressure wave of some amplitude will be closer to the critical point. Since the magnetosonic speed is constructed from both the sound speed ($\sim T^{1/2}$ and Alfvén speed ($\sim B/n^{1/2}$)), we can use Ulysses measurements made while flying over the poles of the Sun (and hence free from the complication of interaction regions) to estimate whether the magnetosonic speed increased or decreased from one minimum to the next. During the recent minimum, the high-speed solar wind was observed to be cooler ($\sim 14\%$) and less dense ($\sim 17\%$) (McComas et al., 2008). More consequentially, the magnetic field was $\sim 36\%$ lower. Thus, the Alfvén speed was $\sim 9\%$ lower and the sound speed was $\sim 4\%$ lower. Jian et al. (2011) also noted that while the number of shocks increased, they were, generally, weaker. If the increase in the number of R shocks was due to the increased strength of the high-speed streams, we would also expect the R shocks to be generally stronger. On the other hand, if it were to a net decrease in the threshold for the wave to actually steepen into a shock, they would not need to be stronger. Moreover, one, or both of these explanations could account for the dip in shock rate surrounding solar maximum: streams at solar maximum are generally weaker but also, the ambient magnetic field strength is larger than during solar minimum (Riley, 2007).

We offer a third explanation for the increase in the number of R shocks during the recent minimum. During the period approaching, and coincident with the previous minimum, R shocks formed at the trailing edges of CIRs that were tilted and offset from the equatorial plane; their tilt being due to either a tilted dipole geometry, or the equatorward expansion of polar coronal holes. Thus, in-ecliptic spacecraft tended to intercept them, if at all, at their flanks. In contrast, during the recent minimum, and as illustrated by Figs. 7–9 the omnipresence of equatorial coronal holes produced high-speed streams, and hence CIRs whose shocks were more equatorially centered. Thus, all other things being equal, we would expect a larger number of R shocks per Carrington rotation.

This explanation also helps us understand the decrease in the ratio of F to R shocks between the two minima (as shown in Fig. 6): While most, or all F CIR-associated shocks were intercepted in the ecliptic, regardless of their origin from tilted stream profiles, equatorward extensions, or equatorial coronal holes, the R shocks were not. Thus, the decrease in the F/R ratio is an increase in the number of R shocks, not a decrease in the number of F shocks, which is essentially confirmed by Fig. 5.

That the ratio of F to R shocks was greater than one almost every year, and over 10 in 1997, is in apparent contradiction to the commonly held view within the scientific community that R shocks associated with CIRs are more likely to form at smaller heliocentric distances than F shocks, and, thus, should be observed more frequently than F shocks. This belief is based on the early 1-D simulations by Hundhausen (1973) (and references therein) who showed that F and R shocks formed at roughly the same time, and therefore, because they bounded a finite-sized interaction region, at different heliocentric distances. Since the R shock is always on the trailing edge of the compression, the implication is that more R shocks would be observed at 1 AU more often than F shocks, in contradiction to the observations.

Our modeling results provide a resolution of this apparent paradox based on the position and orientation of CIRs in the heliosphere. In particular, because CIR dynamics are not centered in the ecliptic, but at latitudes where there are longitudinal gradients in speed back at the Sun, Earth-based spacecraft tend to intercept the CIR structures at their flanks. Thus, except in the case of equatorial coronal holes producing CIRs centered about the equator, we anticipate that F shocks should penetrate to lower latitudes than R shocks. In fact, Ulysses at mid-heliographic

latitudes found the opposite (but consistent) result: As it traveled to higher latitudes F shocks disappeared and only R shocks remained (Gosling et al., 1995). In effect, our study has revealed, albeit less clearly, the reverse phenomena in the ecliptic plane.

Our analysis and comparison with model results has been statistical in the sense that we have not attempted to match each observed SI and/or shock with specific model structures. Moreover, we have not attempted to compute the orientation of the shocks bounding the CIRs and compared them either with the observed shocks or the orientations deduced from the flow deflections at the SIs. Although this might be a useful exercise, based on previous studies, we anticipate that the correlation will be relatively low. F and R shocks, for example, often deviate significantly from the larger-scale orientations of the structures they bound, most likely the result of small-scale corrugations in the shock front (Riley and Sonett, 1996). Current global models are capable, at best, of recovering meso- and large-scale structure, in the absence of any wave or turbulence that would also complicate the matter. Instead, we have probed the model results to understand what features in the global modeling would cause such systematic azimuthal flows, but irregular, or non-existent meridional flows, and a stronger prevalence of F to R shocks, as well as a surge in R shocks during the most recent minimum.

Although we have used a fairly sophisticated MHD model to interpret the patterns (and lack thereof, in some cases) we can appeal to simpler illustrations that perhaps explain the measurements more clearly. In Fig. 10 (top), we have drawn four solar velocity profiles. These spherical surfaces are sufficiently close to the Sun that no substantial interaction has yet taken place, but sufficiently far from the Sun that the flow is essentially radial. Cases (a) and (b) are in

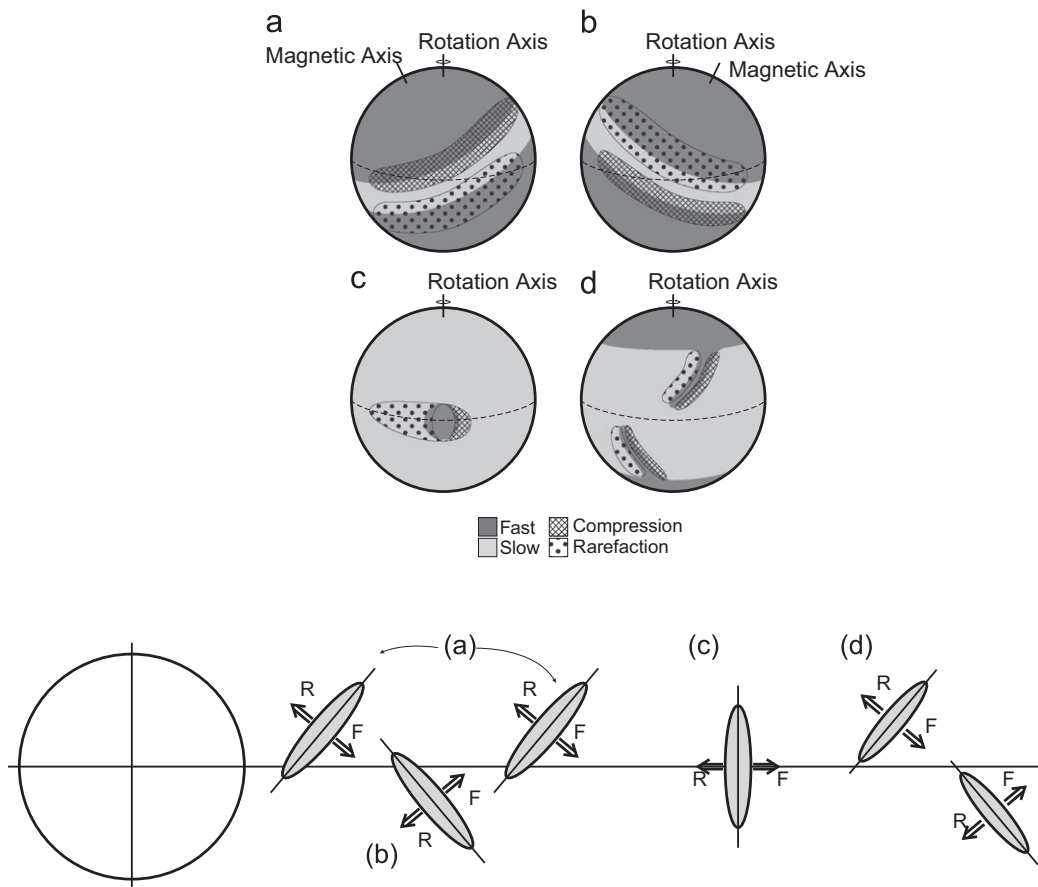


Fig. 10. (Top) An illustration of how different velocity profiles near the Sun (say $30R_{\odot}$) can produce CIRs with particular orientations farther out in the heliosphere (bottom). See text for more details.

fact different views of the same configuration – a tilted dipole, which prevailed during the declining phase of solar cycle 22. Here, a band of slow wind flows out from the magnetic equator, which is tilted with respect to the rotation axis. Focusing on (a) first, slow wind from central meridian is overtaken by faster wind to the east creating a compression region. Similarly, in the southern hemisphere, predominantly fast wind outpaces slower wind to the east creating a rarefaction region. The same processes, but in the opposite hemispheres, occur on the other side of the Sun (b). The bottom part of Fig. 10 shows how these interaction regions (specifically the compression regions) are tilted in the meridional plane, due to the initial gradient of the slow-flow band with respect to heliographic longitude. The F shock bounds the leading edge of the CIR with the R shock trailing it. As drawn, these suggest that, at the least, F shocks intercepted by an in-ecliptic spacecraft will be stronger than the trailing R shock, which will be intercepted further in the flanks of the CIR.

A situation more reminiscent of solar maximum, but also a component of the recent solar minimum is shown in panel (c) of Fig. 10. Here, a fast stream of solar wind emanates from an equatorial coronal hole punching through slower solar wind ahead (originating from the west). A compression region forms on the western edge and a rarefaction trails to the east. Now the orientation of the CIR measured by a spacecraft will depend on its position relative to the center of the coronal hole (or at least the extrapolation of the coronal hole out to our solar wind source radius). However, on average, there will be no systematic tilt, and thus, no meridional deflection of the flow. The F and R shocks will, again on average, be of approximately the same strength. Finally, a third possible configuration is illustrated in panel (d). Typically, such a configuration occurs when well established coronal holes develop an equatorial extension because of a strong but isolated active region at low latitudes, as was the case, for example, at the minimum terminating solar cycle 22 (CR 1913, September 1996). The formation of the compression and rarefaction regions follows a similar explanation as for cases (a)–(c), the main difference here being in how far the CIR penetrates equatorward. Whereas the CIRs in cases (a) and (b) intercepted the equator, in case (d) they would terminate at higher latitudes. Also the tilts of the CIRs and associated shocks would depend on the orientation of the equatorward extension of the hole; in this example producing meridional tilts somewhere between cases (a)/(b) and (c).

In closing, we emphasize that our present study has provided, at best, a statistical interpretation of the Wind/ACE CIR observations. It remains to be seen if the inferences we have drawn hold out on a case by case comparison between measurements and simulation results. These results would, in turn, benefit from a careful analysis of the orientation of the F and R shocks bounding the CIRs.

Acknowledgments

The authors gratefully acknowledge the support of NSF under the Center for Integrated Space Weather Modeling (CISM) program, the LWS Strategic Capabilities Program (NASA, NSF, and AFOSR), NASA's Heliophysics Theory Program (HTP), and the STEREO IMPACT team. Additionally, PR acknowledges support from NASA's Causes and Consequences of the Minimum of Solar Cycle 24 program.

References

- Belcher, J.W., Davis Jr., L., 1971. Large-amplitude Alfvén waves in the interplanetary medium, 2. *Journal of Geophysical Research* 76, 3534–3563.
- Burlaga, L.F., 1974. Interplanetary stream interfaces. *Journal of Geophysical Research* 79, 3717–3725.
- Emery, B.A., Richardson, I.G., Evans, D.S., Rich, F.J., 2009. Solar wind structure sources and periodicities of auroral electron power over three solar cycles. *Journal of Atmospheric and Solar-Terrestrial Physics* 71 (July), 1157–1175.
- Gibson, S.E., de Toma, G., Emery, B., Riley, P., Zhao, L., Elsworth, Y., Leamon, R.J., Lei, J., McIntosh, S., Mewaldt, R.A., Thompson, B.J., Webb, D., 2011. The whole heliosphere interval in the context of a long and structured solar minimum: an overview from sun to earth. *Solar Physics*, doi:10.1007/s11207-011-9921-4, in press.
- González-Esparza, J.A., Smith, E.J., 1997. Three-dimensional nature of interaction regions: Pioneer, Voyager, and Ulysses solar cycle variations from 1 to 5 AU. *Journal of Geophysical Research* 102 (May), 9781–9792.
- Gosling, J.T., 1995. Solar wind corotating interaction regions: the third dimension. *Reviews of Geophysics* 33, 597–602.
- Gosling, J.T., Asbridge, J.R., Bame, S.J., Feldman, W.C., 1978. Solar wind stream interfaces. *Journal of Geophysical Research* 83 (April), 1401.
- Gosling, J.T., Bame, S.J., McComas, D.J., Phillips, J.L., Pizzo, V.J., Goldstein, B.E., Neugebauer, M., Snyder, C.W., 1995. Solar wind corotating stream interaction regions out of the ecliptic plane: Ulysses. *Space Science Review* 72, 99.
- Hundhausen, A.J., 1973. Evolution of large-scale solar wind structures beyond 1 AU. *Journal of Geophysical Research* 78, 2035.
- Jian, L., Russell, C.T., Luhmann, J.G., Skoug, R.M., 2006. Properties of stream interactions at one AU during 1995–2004. *Solar Physics* 239 (December), 337–392.
- Jian, L.K., Russell, C.T., Luhmann, J.G., 2011. Comparing solar minimum 23/24 with historical solar wind records at 1 AU. *Solar Physics*, 155.
- Kirk, M.S., Pesnell, W.D., Young, C.A., Hess Webber, S.A., 2009. Automated detection of EUV polar coronal holes during Solar Cycle 23. *Solar Physics* 257 (June), 99–112.
- McComas, D.J., Ebert, R.W., Elliott, H.A., Goldstein, B.E., Gosling, J.T., Schwadron, N.A., Skoug, R.M., 2008. Weaker solar wind from the polar coronal holes and the whole Sun. *Geophysical Research Letters* 35 (September), 18103.
- Neugebauer, M., Snyder, C.W., 1966. Mariner 2 observations of the solar wind, 1, average properties. *Journal of Geophysical Research* 71 (October), 4469.
- NOAA/SWPC, 2011. Solar Cycle Progression <<http://www.swpc.noaa.gov/SolarCycle/>>.
- Odstrčil, D., Riley, P., Zhao, X.P., 2004. Numerical simulation of the 12 May 1997 interplanetary CME event. *Journal of Geophysical Research* 109 (February), 2116.
- Phillips, T., 2009. Science at NASA: Deep Solar Minimum <<http://science.nasa.gov/>>.
- Pizzo, V.J., 1981. On the application of numerical models to the inverse mapping of solar wind flow structures. *Journal of Geophysical Research* 86 (August), 6685.
- Pizzo, V.J., 1982. A three-dimensional model of corotating streams in the solar wind. III – Magnetohydrodynamic streams. *Journal of Geophysical Research* 87 (June), 4374.
- Pizzo, V.J., 1991. The evolution of corotating stream fronts near the ecliptic plane in the inner solar system. II – Three-dimensional tilted-dipole fronts. *Journal of Geophysical Research* 96 (April), 5405–5420.
- Riley, P., 2007. An alternative interpretation of the relationship between the inferred open solar flux and the interplanetary magnetic field. *Astrophysical Journal Letters* 667 (September), L97–L100.
- Riley, P., 2010. The three-dimensional structure of the inner heliosphere. In: Maksimovic, M., Issautier, K., Meyer-Vernet, N., Moncuquet, M., Pantellini, F. (Eds.), Twelfth International Solar Wind Conference, American Institute of Physics Conference Proceedings, vol. 1216; 2010, pp. 323.
- Riley, P., Gosling, J.T., Weiss, L.A., Pizzo, V.J., 1996. The tilts of corotating interaction regions at mid heliographic latitudes. *Journal of Geophysical Research* 101 (A11), 24349.
- Riley, P., Linker, J.A., Lionello, R., Mikić, Z. Corotating Interaction Regions during the Recent Solar Minimum: The Power and Limitations of Global MHD Modeling. *Journal of Atmospheric and Terrestrial Physics*, doi:10.1016/j.jastp.2011.12.013, in press.
- Riley, P., Linker, J.A., Mikić, Z., 2001. An empirically driven global MHD model of the corona and inner heliosphere. *Journal of Geophysical Research* 106, 15889.
- Riley, P., Linker, J.A., Mikić, Z., 2002. Modeling the heliospheric current sheet: Solar cycle variations. *Journal of Geophysical Research* 107 (A7). doi:10.1029/2001JA000299.
- Riley, P., Linker, J.A., Mikić, Z., 2010. Global MHD modeling of the solar corona and inner heliosphere for the whole heliosphere interval. *Highlights of Astronomy* 15, 491–493.
- Riley, P., Linker, J.A., Mikić, Z., Odstrčil, D., Zurbuchen, T.H., Lario, D., Lepping, R.P., 2003a. Using an MHD simulation to interpret the global context of a coronal mass ejection observed by two spacecraft. *Journal of Geophysical Research* 108, 2.
- Riley, P., Lionello, R., Linker, J.A., Mikić, Z., Luhmann, J., Wijaya, J., 2011. Global MHD modeling of the solar corona and inner heliosphere for the whole heliosphere interval. *Solar Physics*, 145.
- Riley, P., Luhmann, J.G., 2011. Interplanetary Signatures of Unipolar Streamers and the Origin of the Slow Solar Wind. *Solar Physics*, doi:10.1007/s11207-011-9909-0, in press.
- Riley, P., Mikić, Z., Linker, J.A., 2003b. Dynamical evolution of the inner heliosphere approaching solar activity maximum: interpreting Ulysses observations using a global MHD model. *Annals of Geophysics* 21, 1347.
- Riley, P., Sonett, C.P., 1996. Interplanetary observations of solar g-mode oscillations? *Geophysical Research Letters* 23, 1541–1544.

- Russell, C.T., Shinde, A.A., Jian, L., 2005. A new parameter to define interplanetary coronal mass ejections. *Advances in Space Research* 35, 2178–2184.
- Sarabhai, V., 1963. Some consequences of nonuniformity of solar wind velocity. *Journal of Geophysical Research* 68, 1555.
- Siscoe, G.L., 1972. Structure and orientation of solar-wind interaction fronts: Pioneer 6. *Journal of Geophysical Research* 77, 27–34.
- Sonett, C.P., Colburn, D.S., 1965. The $SI^+ - SI^-$ pair and interplanetary forward-reverse shock ensembles. *Planetary and Space Science* 13 (July), 675.
- Stevens, M., Linker, J.A., Riley, P. A study of the sensitivity of global MHD model solutions of the solar corona to boundary conditions. *Journal of Atmospheric and Terrestrial Physics*, submitted for publication.
- Svalgaard, L., Cliver, E.W., 2007. A floor in the solar wind magnetic field. *Astrophysical Journal Letters* 661 (June), 203.
- Wimmer-Schweingruber, R.F., von Steiger, R., Paerli, R., 1997. Solar wind stream interfaces in corotating interaction regions: SWICS/Ulysses results. *Journal of Geophysical Research* 1021 (August), 17407–17418.